SCIENTIFIC REPORTS

OPEN

Received: 28 October 2016
Accepted: 15 December 2016
Published: 24 January 2017

Cu*Mn*OS Nanoflowers with Different Cu^{+}/Cu^{2+} Ratios for the CO_2-to-CH_3OH and the CH_3OH-to-H_2 Redox Reactions

Xiaoyun Chen[1,2], Hairus Abdullah[1] & Dong-Hau Kuo[1]

A conservative CO_2-Methanol (CH_3OH) regeneration cycle, to capture and reutilize the greenhouse gas of CO_2 by aqueous hydrogenation for industry-useful CH_3OH and to convert aqueous CH_3OH solution by dehydrogenation for the clean energy of hydrogen (H_2), is demonstrated at normal temperature and pressure (NTP) with two kinds of Cu*Mn*OS nanoflower catalysts. The [Cu^{+}]-high Cu*Mn*OS led to a CH_3OH yield of 21.1 mmol·g^{-1}catal.·h^{-1} in the Cu*Mn*OS-CO_2-H_2O system and the other [Cu^{+}]-low one had a H_2 yield of 7.65 mmol·g^{-1}catal.·h^{-1} in the Cu*Mn*OS-CH_3OH-H_2O system. The successful redox reactions at NTP rely on active lattice oxygen of Cu*Mn*OS catalysts and its charge (hole or electron) transfer ability between Cu^{+} and Cu^{2+}. The CO_2-hydrogenated CH_3OH in aqueous solution is not only a fuel but also an ideal liquid hydrogen storage system for transportation application.

Clean and renewable energies such as solar, wind, hydraulic, hydrogen, biomass energies can partially substitute for fossil fuels for the sakes of the depletion in oil resources and the emissions in greenhouse gas. The methanol economy advocated by Nobel prize winner George A. Olah in 1990 s has been promising as CH_3OH is not only a good hydrogen liquid carrier but also a key industrial chemical feedstock[1,2]. The success in methanol economy is related to the reversible CO_2 hydrogenation-CH_3OH dehydrogenation or the CO_2-CH_3OH cycle. In this way, the underground fossil carbon can be conservatively exploited.

CO_2 hydrogenation by the thermochemical conversion of the mixture of $CO/CO_2/H_2$ (termed "syngas") for CH_3OH operates at high temperature of ~250 °C and high pressures of ~50 bar over copper-based heterogeneous catalysts in an industrial production scale[3–5]. Studt *et al.* discovered a stable Ni-Ga alloy catalyst that reduced CO_2 to methanol at ambient pressure[6]. As CO_2 conversion to methanol is a thermodynamically exergonic process, the Ni-Ga catalyzed conversion of CO_2 to methanol needs to be operated at and above 200 °C. To process at a mild condition, the homogeneous catalysis mainly with the use of ruthenium- and iridium-based complexes for CO_2 hydrogenation is being developed below 145 °C under a high pressure of 60 bars[7–9]. Photocatalysis for CO_2 conversion to methanol in water under high power lamp with sulfide/sulfate reagents is still an active research area[10–12]. Liu *et al.* demonstrated the good performance with a Cu/CeO_2/doped graphene catalyst, but they needed the 250 W lamp illumination and Na_2SiO_3 reagent.

CH_3OH dehydrogenation for hydrogen (H_2) currently perform through steam reforming over the heterogeneous $CuO/ZnO/Al_2O_3$ catalyst at 200–300 °C[13–15]. The lower reaction temperature of 65–150 °C has been achieved with the active homogeneous ruthenium-complex catalysts, but additional reagents are needed[4,16,17]. Photocatalysis for aqueous alcohol conversion with a large amount of hydrogen has been achieved under high power lamp, Pt, CdS, or sulfate reagent[18–20]. A low operation temperature for alcohol dehydrogenation can be key factor to make CH_3OH suitable as energy liquid carrier for portable and vehicle applications.

High temperature and pressure conversion reaction, high illumination intensity, external electrical energy input, and complex reagents have been the major approaches to make parts of the CO_2-CH_3OH cycle feasible for effective energy and environment managements. Therefore, the energy supplies from the perennial sources such as sun, wind, and geothermal to execute the reactions for fuels and chemicals have been widely pursued. Recently, metallic AgPd hollow sphere anchored on graphene demonstrated the dehydrogenation of formic acid for H_2 at room temperature[21]. It is encouraging that the catalytic reaction with AgPd for H_2 production without thermal,

[1]Department of Materials Science and Engineering, National Taiwan University of Science and Technology, Taipei 10607, Taiwan. [2]College of Material Engineering, Fujian Agriculture & Forestry University, Fuzhou 350002, China. Correspondence and requests for materials should be addressed to D.-H.K. (email: dhkuo@mail.ntust.edu.tw)

electrical, and photo energies is not impossible to occur. Here, we demonstrate two kinds of inorganic Cu*Mn*OS catalysts with low cost: the [Cu^+]-high Cu*Mn*OS acts as catalyst to accelerate the reduction reaction of the CO_2 hydrogenation to methanol and the [Cu^+]-low Cu*Mn*OS to speed up the oxidation reaction of the methanol dehydrogenation into hydrogen and carbon dioxide, to complete the conservative CO_2-CH_3OH cycle at normal temperature and pressure without additional reagents.

Methods

Synthesis of CuMnOS. To prepare Cu*Mn*OS powder, 1.5 g thioacetamide (CH_3CSNH_2) was added into a 500 ml solution with cupric nitrate ($Cu(NO_3)_2{\cdot}2.5H_2O$) and manganese (II) chloride ($MnCl_2$) in the weight ratio of 1: 1, followed by 30 min stirring. Then the mixture solution was steadily heated to 95 °C and 0.0, 0.1, 0.2, 0.3 and 0.4 ml hydrazine (N_2H_4) were added to prepare the powders at different redox conditions. After stirring for 2 h, the precipitates were collected after centrifugation and washing procedures. The precipitates were dried in oven at 80 °C for 24 h. The obtained catalysts were labeled as Cu*Mn*OS-0, Cu*Mn*OS-1, Cu*Mn*OS-2, Cu*Mn*OS-3, and Cu*Mn*OS-4, depending upon their N_2H_4 content. For comparative purpose, the CuOS was prepared at the same procedure without adding $MnCl_2$.

Characterization of CuMnOS. The photoelectron spectrometry (XPS) was proceeded with VG Scientific ESCALAB 250 XPS under the Al Kα X-rays ($h\nu = 1486.6$ eV) radiation and calibrated with carbon C1*s* ($Ea = 284.62$ eV). The X-ray powder diffraction (XRD) study was conducted on Bruker D2 phaser X-ray diffractometry at 10 kV using Cu Kα radiation at a scanning step size of 0.05° and with residence time of 0.5 min. SEM images were obtained from JSM-7610F field-emission scanning electron microscope (FE-SEM) operated at an accelerating voltage of 15 kV. A Tecnai F20 G2 instrument was used to obtain the TEM images and microstructural information. To obtain the specific surface area (S_{BET}), N_2 adsorption-desorption experiments were performed on Micromeritics ASAP 2020 porosity and specific surface area analyzer after the sample degassed at 150 °C for 2 h. UV-Vis DRS was evaluated on a JASCD V-670 UV-Vis spectrophotometer with an integrating sphere of 60 mm and $BaSO_4$ as a reference material. Photoluminescence (PL) emission spectrum was measured at room temperature on JASCD FB-8500 fluorescence spectrophotometer with a laser beam at 330 nm emission wavelength.

Reduction/hydrogenation reactions. *Reduction of Cr(VI) by the catalytic reduction reaction of CuMnOS.* To execute the reduction of Cr(VI), the 50 mg catalyst was added into the reactor filled with 100 mL Cr(VI) solution of 50 mg/L. The reactor also was wrapped with aluminum foil. After reaction for 2 min, approximately 8 mL sample was taken out and passed through a 0.45 μm membrane filter syringe to immediately separate catalysts from the solution. The diphenycarbazide (DPC) colorimetric method[22] with JASCD V-670 spectrophotometer and the ion chromatography (IC) method with Thermo ICS-5000 spectrophotometer were used to determine the Cr(VI) concentration in filtrate. To evaluate the reusability, the catalysts after the first run were re-used for the second run at the same condition after re-filling with a fresh Cr(VI) solution without being washed. For this reusability purpose, a larger amount of 50 mg catalyst was used to avoid the larger deviation caused by the weight loss.

Reduction conversion of CO_2 by aqueous hydrogenation with CuMnOS catalyst. Reduction conversion of CO_2 to CH_3OH with Cu*Mn*OS was carried out in a home-made and jacketed quartz reactor wrapped by aluminum foil. For each run, the 0.1 g catalyst was added into the reactor with 70 mL distilled water, then CO_2 gas, released from $NaHCO_3$ solution by controlling the addition of dilute HNO_3 aqueous solution, was passed into the reactor under the ambient laboratory condition. The whole procedure lasted for 18 h. The products were collected and analyzed by GC with flame ionization detector (FID).

Oxidation/dehydrogenation reactions. *Degradation of methylene blue by dye oxidation reaction with CuMnOS catalyst.* To proceed the MB degradation experiments, the 25 mg catalyst was added into the reactor filled with 100 mL MB solution of 10 mg/L. The reactor was wrapped with aluminum foil to exclude the effects of UV and visible light irradiations. The 3 mL sample was taken out from the reactor every 5 min, followed by instant centrifugation in 1 min. The supernatant absorbance was measured with a JASCD V-670 UV-Vis spectrophotometer for peak located at 663 nm. Their concentration was calculated based on the Lambert-Beer law. To evaluate the reusability, the catalysts after the first run were re-used for the second run at the same condition after re-filling with a fresh MB solution without being washed.

Hydrogen generation by catalytic dehydrogenation (aqueous oxidation) with CuMnOS. Hydrogen generation was conducted in a home-made and jacketed quartz reactor equipped with the input and output valves to control the gas flow. To exclude the visible light irradiation, the reactor was wrapped by aluminum foil. One Cu*Mn*OS sample was compared by exposure under the 150 W Halogen lamp illumination. The input valve was connected to a gas tank of 99.99% Ar and the output one to a well-callibrated gas chromatography (GC) with thermal conduction detector (TCD) system. The hydrogen evolution experiment was carried out with the well-dispersed 225 mg catalyst in 450 mL pure ethanol (C_2H_5OH), water, ethanoic acid, or the methanol (CH_3OH), ethanol, or ethanoic acid aqueous solution (20% v/v). The gas sampling was taken for each time interval of 20 min. Gas sampling was conducted by flowing Ar gas through the reactor to GC-TCD system for several minutes. A hydrogen calibration line was built to quantitatively measure the H_2 generation rate.

Results

XPS analysis. The compositions of Cu*Mn*OS-0 and Cu*Mn*OS-3 are listed in Table 1 after the XPS analyses. The Cu, Mn, O, and S contents are close for the two kinds of catalysts prepared at different N_2H_4 contents.

Catalyst	Molar percentage				Cu molar percentage		Cu^+/Cu^{2+} molar ratio	O-bonding molar percentage			S molar percentage		S^{6+}/S^{2-} molar ratio	O^2/S^{2-} molar ratio
	Cu	Mn	O	S	Cu^+	Cu^{2+}		O-H	O-Cu^+ O-Mn	O-Cu^{2+}	S^{6+}	S^{2-}		
Cu*Mn*OS-0	39.6	1.6	21.9	36.9	59.8	40.2	1.49	32.3	33.3	34.4	13.5	86.5	0.156	0.465
Cu*Mn*OS-3	39.0	1.5	21.3	38.2	70.5	29.5	2.39	31.6	35.1	33.3	18.3	81.7	0.224	0.467

Table 1. XPS composition analyses of Cu*Mn*OS catalysts.

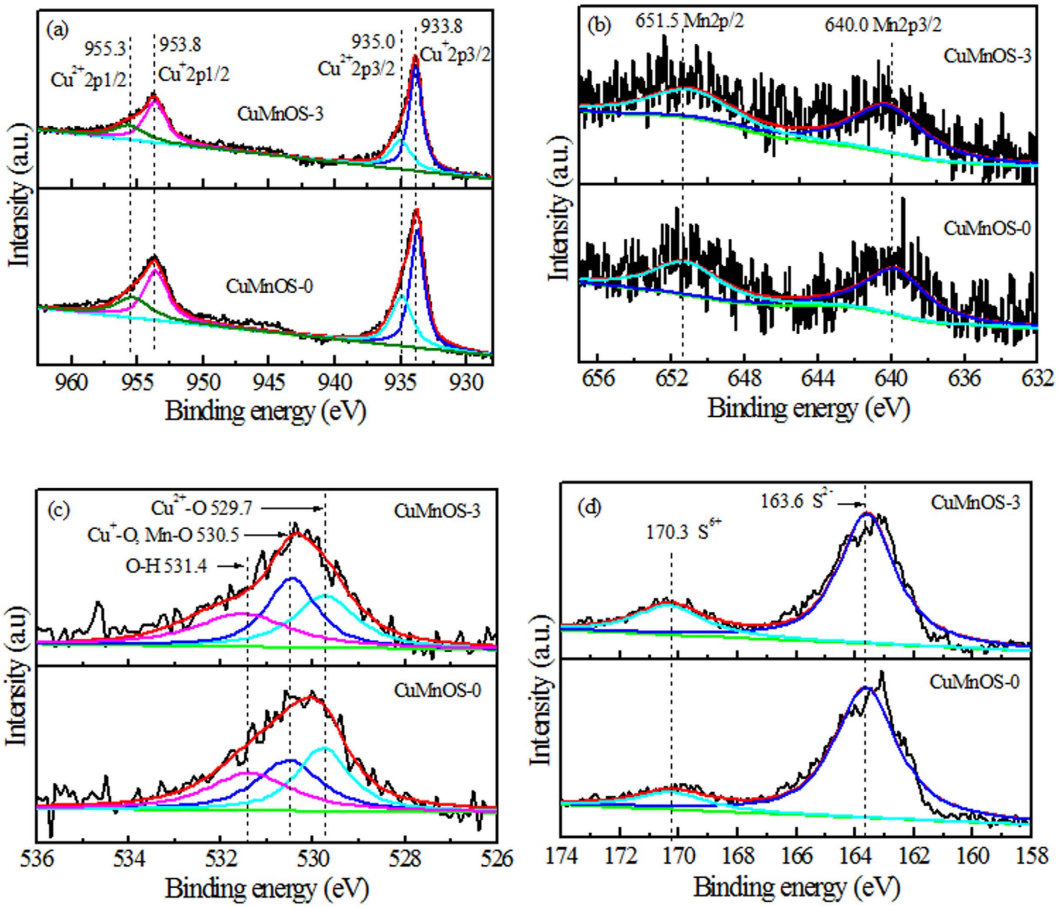

Figure 1. High resolution (**a**) Cu2*p*, (**b**) Mn2*p*, (**c**) O1*s*, and (**d**) S2*p* XPS spectra of Cu*Mn*OS-0 and Cu*Mn*OS-3.

The substitutional Mn has a Mn/(Mn + Cu) molar ratio of ~0.038, a much lower content than the Cu content. Figure 1a shows the high resolution Cu2*p* XPS spectra of Cu*Mn*OS-0 and Cu*Mn*OS-3. The asymmetric Cu2*p* peaks were contributed to the different chemical states of Cu in Cu*Mn*OS. The peak separation of 20.0 eV between Cu2*p*3/2 and Cu2*p*1/2 located at 933.8 eV and 953.8 eV, respectively, indicates that copper is for the monovalent Cu^{+}[23]. The peaks of 2*p*3/2 and 2*p*1/2 located at 935.0 eV and 955.3 eV, respectively, were attributed to the spin-orbit splitting of the bivalent Cu^{2+}[24,25]. According to the quantitative analysis by integrating the peak area, both of catalysts are richer in Cu^+ than Cu^{2+} and the Cu^+/Cu^{2+} molar ratios were calculated to be 1.49 for Cu*Mn*OS-0 and 2.39 for Cu*Mn*OS-3. With increasing the reducing N_2H_4 content, the Cu^+/Cu^{2+} molar ratio increased or the $Cu^{2+} \rightarrow Cu^+$ transition was accelerated. Cu*Mn*OS-0 without adding N_2H_4 has a lower Cu^+ content and it is labeled as [Cu^+]-low Cu*Mn*OS. Cu*Mn*OS-3 had a higher Cu^+ content after adding N_2H_4 during the preparation stage and it is labeled as [Cu^+]-high Cu*Mn*OS.

Figure 1b shows the high resolution Mn2*p* XPS *spectra* of Cu*Mn*OS-0 and Cu*Mn*OS-3. The peak separation of 11.5 eV between Mn2*p*3/2 and Mn2*p*1/2 located at 640.0 eV and 651.5 eV, respectively, indicates that copper is for the bivalent Mn^{2+}[26,27]. Figure 1c shows the high resolution O1*s* XPS spectra of Cu*Mn*OS. The asymmetric O1*s* peak was convoluted into three kinds of peaks at 531.4 eV contributing from the hydroxyl oxygen[28], at 530.5 eV from the Mn-O and monovalent Cu^+ -O[29,30], and 529.7 eV from the bivalent Cu^{2+} -O[31]. Figure 1d shows the high resolution S2*p* XPS spectra of Cu*Mn*OS. The S2*p* peaks at 163.6 eV belongs to the S^{2-}[32,33] and at 170.3 eV to S^{6+}[34]. With increasing the reducing N_2H_4 content, the S^{6+} content in Cu*Mn*OS, for the sake of charge neutrality, increases to compensate the loss in the positive charge due to the $Cu^{2+} \rightarrow Cu^+$ transition. That is to say, [Cu^+]-low

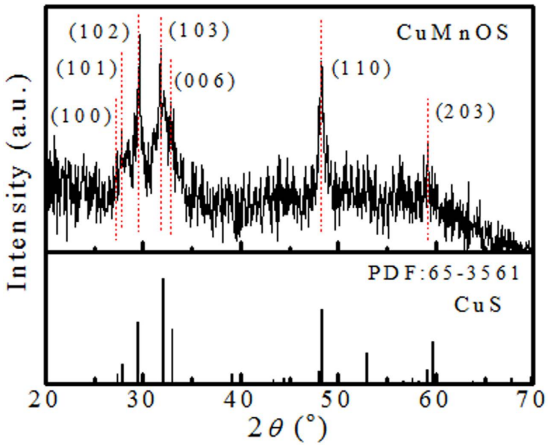

Figure 2. XRD pattern of Cu*Mn*OS catalyst, together with the standard peak positions of CuS.

Cu*Mn*OS-0 has a lower S^{6+} content and [Cu^{+}]-high Cu*Mn*OS-3 a higher one. The Cu^{+} content is proportional to the S^{6+} content in Cu*Mn*OS. The lattice O^{-2}/S^{-2} molar ratio, removing the contribution from the hydroxyl oxygen, is ~0.466 for both of catalysts with a slightly higher S^{2-} ratio.

XRD analysis. Figure 2 shows the XRD diffraction pattern of Cu*Mn*OS and the standard peaks of CuS based upon PDF # 65-3561. The diffraction peaks of Cu*Mn*OS-0 were the same as those of Cu*Mn*OS-3. XRD peak positions of Cu*Mn*OS were well matched to those of the hexagonal CuS covellite structure. The main peaks located at 27.66°, 28.36°, 29.62°, 31.81°, 32.72°, 48.23°, and 59.15° attributed to the (100), (101), (102), (103), (006), (110), and (203) crystal planes, respectively. The weak and broad Cu*Mn*OS peaks are attributed to the poor crystallization. XRD diffraction pattern did not show any second phase.

SEM and TEM microstructural and structural analyses. Figure 3a shows the FE-SEM images of Cu*Mn*OS-3. Cu*Mn*OS looks like the petal-gathered nanoflower particles with its size of 300~500 nm. Similar to Cu*Mn*OS-3 in FE-SEM image, Cu*Mn*OS-0 was not displayed. Figure 3b shows the TEM image of Cu*Mn*OS to further verify its nanoflower-like microstructure. The inset in Fig. 3b shows the image at higher magnification. Figure 3c shows the HR-TEM image of Cu*Mn*OS. Different lattice fringes belonging to different grains were observed, indicating the nature of nanoparticles. Figure 3d shows the selected area electron diffraction (SAED) pattern of Cu*Mn*OS-3. The ring patterns from the (102), (103), (110) and (203) planes explain its polycrystalline nature. The scattered ring pattern explains the solid solution nature of Cu*Mn*OS. Figure 3e gives the HAADF-STEM image, which reveals many pores with different sizes inside the nanoflower-like Cu*Mn*OS particles. Figure 3f shows the FE-SEM-EDS spectrum, which verifies that aggregates are composed of Cu, Mn, S, and O. Figure 3g–j show the HAADF-STEM-EDX elemental maps of Cu, Mn, O, and S. From these element mappings, we can confirm the composition uniformity in samples.

UV-Vis absorption and photoluminescence. The optical absorption property of Cu*Mn*OS was characterized by UV-Vis absorption spectroscopy. Cu*Mn*OS had a better visible light absorbance than CuOS. From the UV-Vis spectra, the direct band gap was measured with the equation versus photon energy ($h\nu$)[35]:

$$(\alpha h\nu)^2 = k(h\nu - E_g)$$

where α is the absorbance coefficient, h the Planck constant, k the absorption constant for a direct transition, $h\nu$ the absorption energy, and E_g the band gap. Figure 4a shows the $(\alpha h\nu)^2$-$h\nu$ curves of Cu*Mn*OS together with the comparative CuOS. The E_g values were determined to be 2.0 eV for CuOS and 1.5~1.6 eV for Cu*Mn*OS with the higher value at the higher Cu^{+} content in Cu*Mn*OS. The variation of energy band gap further indicates that Cu*Mn*OS is a bimetal oxysulfide solid solution instead of monocrystalline CuO with band gap of $E_g = 1.2$–1.4 eV, Cu_2O of 2.0–2.2 eV, CuS of 2.15–2.36 eV, and Cu_2S of 1.2–1.25 eV.

Figure 4b shows PL spectra of the Cu*Mn*OS catalysts. Under a laser beam at wavelength of 330 nm, catalysts were excited with PL spectra at about 593 nm. The peak at 660 nm is originated from the laser contribution. It is observed that the 593 nm peak intensity increases with the N_2H_4-adding content or the Cu^{+} content. The more Cu^{+} content in Cu*Mn*OS-3 can contribute the more defect levels to lead to the higher emission intensity.

BET and pore size analyses. Figure 5a shows the N_2 adsorption-desorption isotherm of Cu*Mn*OS, which displays the type IV isotherm with the hysteresis loop at relative pressure (P/P_0) between 0.75 and 1.0, indicating its mesoporous feature[36]. Figure 5b shows the pore size distribution of Cu*Mn*OS. Cu*Mn*OS-0 and Cu*Mn*OS-3 had the surface area (S_{BET}) of 20.3 and 18.6 m^2/g, the total pore volumes of 0.151 and 0.141 cm^3/g, and the average pore diameters of 30.5 and 30.4 nm, respectively. The large pore diameter is attributed to the aggregation of the petal-gathered nanoflower particles.

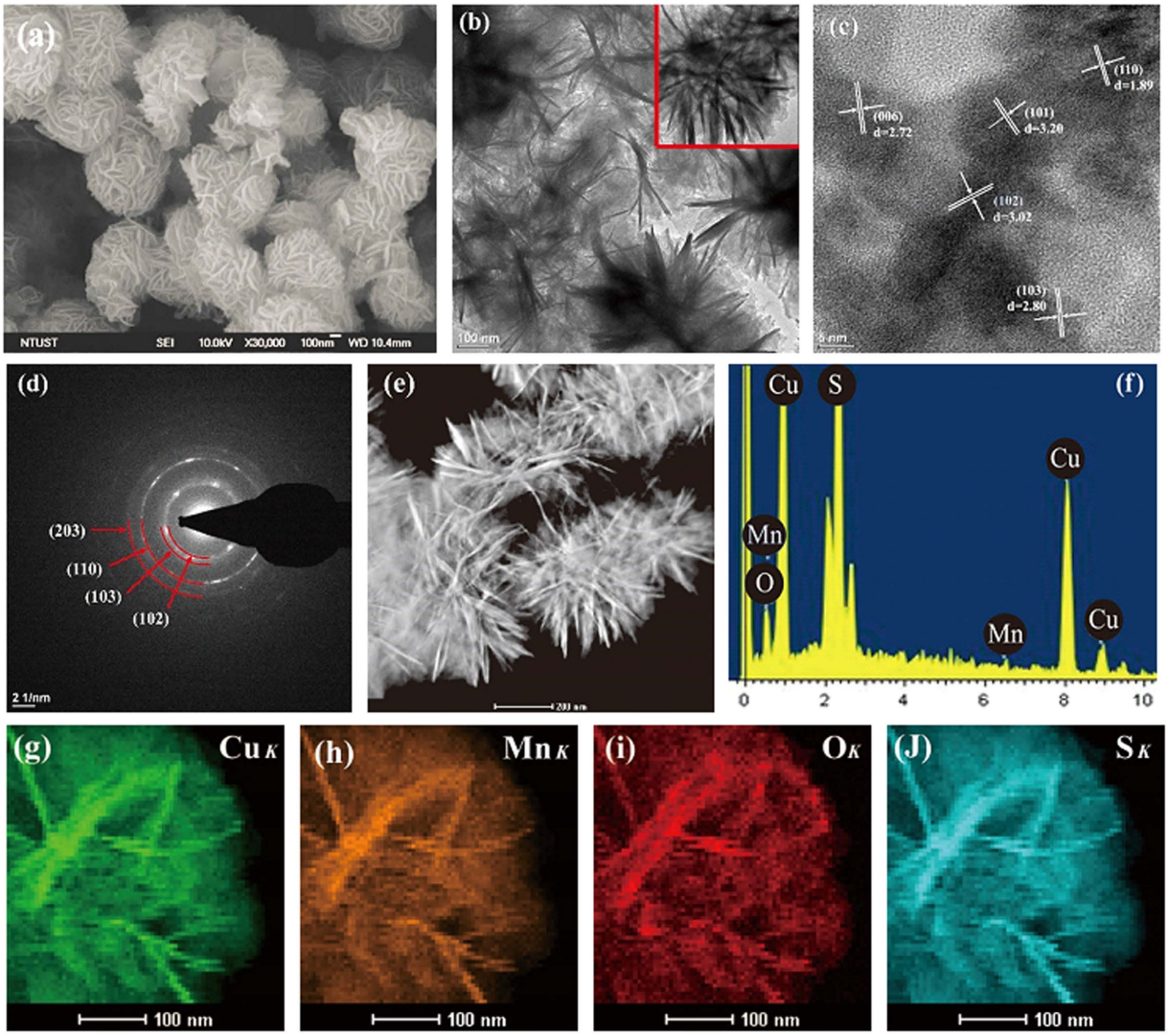

Figure 3. Microstructural and structural characterizations of Cu*Mn*OS-3. (**a**) FE-SEM image, (**b**) TEM image, (**c**) HR-TEM image, (**d**) SAED pattern, (**e**) HAADF-STEM image, (**f**) FE-SEM-EDS spectrum, (**g**–**j**) EDX elemental mapping of Cu, Mn, O, and S, respectively. The inset in (**b**) is for image at higher magnification.

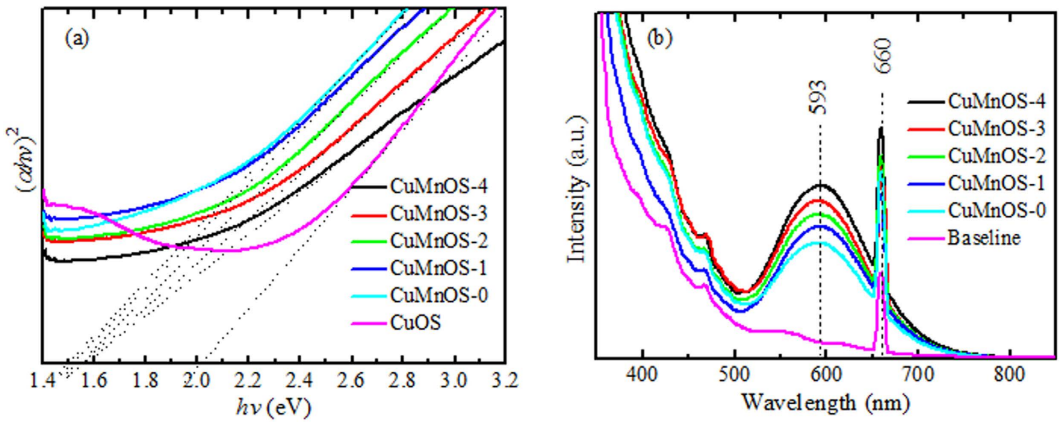

Figure 4. (**a**) the $(\alpha h\nu)^2$-$h\nu$ plot from the optical absorption measurements for determining the bandgap, and (**b**) PL spectra of Cu*Mn*OS catalysts prepared at different N_2H_4 contents.

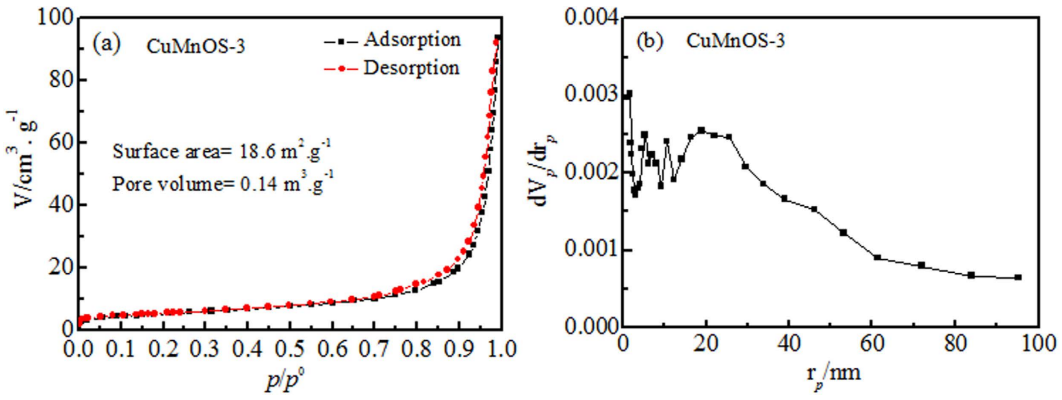

Figure 5. (**a**) Nitrogen adsorption-desorption isotherm and (**b**) pore size distribution curve of Cu*Mn*OS.

Catalyst	CuOS	Cu*Mn*OS-0	Cu*Mn*OS-1	Cu*Mn*OS-2	Cu*Mn*OS-3	Cu*Mn*OS-4
Reduction content (%)	8.5	57.4	80.3	98.9	100	100

Table 2. Catalytic reduction of Cr(VI) with Cu*Mn*OS and CuOS catalysts in the dark.

Catalyst	CuOS	Cu*Mn*OS-0	Cu*Mn*OS-1	Cu*Mn*OS-2	Cu*Mn*OS-3	Cu*Mn*OS-4
CH_3OH yield	0.0	7.4	15.9	17.2	21.1	10.4

Table 3. Cu*Mn*OS catalysts on the reduction of CO_2 in the dark. Note: Unit for the yield: mmol·g^{-1}catal.·h^{-1}.

Reduction activity of CuMnOS on Cr(VI). Table 2 shows the reduction of Cr(VI) over Cu*Mn*OS and CuOS catalysts in the dark. The different Cu*Mn*OS catalysts performed differently in Cr(VI) reduction with the efficiency in the order: Cu*Mn*OS-4 ≈ Cu*Mn*OS-3 > Cu*Mn*OS-2 > Cu*Mn*OS-1 > Cu*Mn*OS-0 > CuOS. The Cu*Mn*OS-3 and Cu*Mn*OS-4 catalysts completed the Cr(VI) reduction in 2 min, while CuOS only completed 8.5%. As tested by IC method, the Cr(VI) in solution was confirmed to be reduced to Cr^0 without the existence of Cr^{3+}. In order to test the catalytic capability and their reusability, Cu*Mn*OS was continuously tested for three runs. After the 3rd run, the Cu*Mn*OS-3 still maintained the good catalytic activity to reduce more than 97.4% of Cr(VI). The results indicate that the bimetal [Cu^+]-high Cu*Mn*OS oxysulfide catalysts prepared with a higher N_2H_4 amount show excellent catalytic activity without the needs of other chemicals and photo energy. The [Cu^+]-high Cu*Mn*OS is promising for industrial applications in Cr(VI) waste water treatment.

The experimental methods for Cr(VI) depollution include photocatalysis and absorption with high surface energy nanomaterials. As the rate constant is affected by the catalyst amount, illumination light intensity etc., the quantity of $K_2Cr_2O_7$ amount (mg) divided by catalyst amount (mg), i.e. $W_{2,(K2Cr2O7)}/W_{1,(catalyst)}$, is used for comparison. Under the UV light, TiO_2-CNT with a W_2/W_1 value of 0.013 reduced 100% Cr(VI) in 40 min[37]. Under the visible light, $Fe_2O_3/g\text{-}C_3N_4$ with a W_2/W_1 value of 0.014 reduced 100% Cr(VI) in 15 min[38]. With no light illumination, diamino pyridine-modified grapheme oxide with a W_2/W_1 value of 0.5 absorbed 94.5% Cr(VI) in 90 min at the help of the electrostatic force[39]. In the dark condition, our Cu*Mn*OS with a W_2/W_1 value of 0.1 reduced Cr(VI) in 2 min. The Cu*Mn*OS catalyst had demonstrated the excellent ability in the reduction of Cr(VI).

Aqueous hydrogenation conversion of CO_2. Table 3 shows the yields of CH_3OH in conversion of CO_2 over Cu*Mn*OS and CuOS. It is interesting to note that pure CuOS did not produce CH_3OH. However, the aqueous hydrogenation of CO_2 by Cu*Mn*OS to produce CH_3OH with the yield in the order: Cu*Mn*OS-3 > Cu*Mn*OS-2 > Cu*Mn*OS-1 > Cu*Mn*OS-4 > Cu*Mn*OS-0. The CH_3OH yield increased with the Cu^+ content in Cu*Mn*OS but reached the highest yield of 21.1 mmol·g^{-1}catal.·h^{-1} at Cu*Mn*OS-3. The [Cu^+]-high Cu*Mn*OS favors the aqueous hydrogenation of CO_2. In the industrial scale, thermal conversion above 200 °C had a rate above 60 mmol·g^{-1}catal.·h^{-1}[40]. For photo conversion, the maximal rate of 0.51 mmol·g^{-1}catal.·h^{-1} was achieved by the Cu-CeO_2 system with the 250 W Xe lamp[10]. Our production in the dark with a rate of 21.1 mmol·g^{-1}catal.·h^{-1} is quite promising.

Degradation of methylene blue by oxidation reaction. Figure 6 shows the degradation of MB over different catalysts in the dark. It is noted that N_2H_4 added in processing has an important effect for preparing Cu*Mn*OS on the degradation of MB with the efficiency in the order: Cu*Mn*OS-0 ≈ Cu*Mn*OS-1 > Cu*Mn*OS-2 > Cu*Mn*OS-3 > Cu*Mn*OS-4. Cu*Mn*OS-0 and Cu*Mn*OS-1 could completely degrade MB in 5 min. However, the CuOS catalyst only removed 9.9% MB in 30 min. In order to test the catalyst reusability, the supernatant of Cu*Mn*OS-0 catalyst after the first test and gravity setting was decanted and then the fresh 100 mL MB solution of 10 ppm was added for the reuse test in the dark without washing catalysts. The 2nd run was also completed in

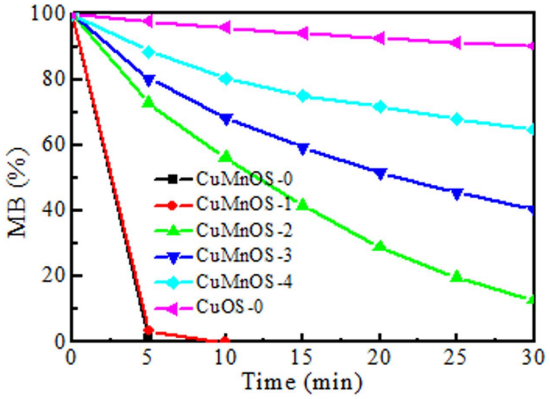

Figure 6. Degradation of MB over Cu*Mn*OS catalysts in the dark.

Condition / Catalyst	Dark/Light	20% methanol + H_2O	20% ethanol + H_2O	20% ethanoic acid + H_2O	H_2O	ethanol
CuOS	Dark	0.27	0.23	—	0	0
Cu*Mn*OS-0	Dark	1.54	8.54	2.17	0	0
Cu*Mn*OS-1	Dark	7.65	9.45	—	0	0
Cu*Mn*OS-2	Dark	1.05	2.13	—	—	—
Cu*Mn*OS-3	Dark	2.24	2.03	—	—	—
Cu*Mn*OS-4	Dark	1.65	2.26	—	—	—
Cu*Mn*OS-0	Visible	2.04	2.45	—	—	—
Cu*Mn*OS-0-200	Dark	1.20	—	—	—	—

Table 4. Hydrogen yields over Cu*Mn*OS under different conditions Note: Unit for the yield: $mmol{\cdot}g^{-1}catal.{\cdot}h^{-1}$; Cu*Mn*OS-0-200: 200 °C-annealed Cu*Mn*OS.

5 min. After the 3rd run, the Cu*Mn*OS remained effective to degrade 95% MB in 5 min. To differentiate the dye degradation or adsorption, the wash-out ethanol solution of Cu*Mn*OS powder after the 3rd run was analyzed with UV-Vis spectrophotometer at 663 nm. The disappearance of the characteristic peak confirmed there was no MB absorption on Cu*Mn*OS. A comparative experiment on activated carbon with S_{BET} above 1000 m^2/g did show the characteristic peak at 663 nm for MB after the carbon powder was washed. Our Cu*Mn*OS has a too low S_{BET} value of ~20 m^2/g for adsorption to proceed, so the MB dye here looks to be degraded by the catalytic reaction in the dark. Together with the XPS data, the $[Cu^+]$-low Cu*Mn*OS dominates over $[Cu^+]$-high one for the MB oxidative degradation.

There are some reports on the MB degradation in the dark. The quantity of MB amount (mg) divided by catalyst amount (mg), $W_{2,(MB)}/W_{1,(catalyst)}$, is used for evaluation. Ag-In-Ni-S nanocomposites with a W_2/W_1 value of 0.0022 degraded 98% MB in 12 min[41]. NiS nanoparticles with a W_2/W_1 value of 0.0089 degraded 100% MB in 15 min[42]. CuS caved superstructure with a W_2/W_1 value of 0.01 degraded 100% MB in 15 min with the help of hydrogen peroxide[43]. Our Cu*Mn*OS with a W_2/W_1 value of 0.04 degraded 100% MB in 5 min. The Cu*Mn*OS catalyst had demonstrated the admirable ability in the degradation of MB.

Hydrogen production by aqueous CH_3OH dehydrogenation. The results of hydrogen production by aqueous CH_3OH dehydrogenation with the Cu*Mn*OS catalysts prepared at different N_2H_4 contents are shown in Table 4. It is interesting to mention that the catalyst in each pure H_2O, alcohol, and organic acid did not generate hydrogen, but the aqueous solutions of alcohol and organic acid produced H_2 at NTP in the dark. For the mixture solution of alcohol and organic acid without water, it did not work out for H_2 generation, either. These results indicate that hydrogen generation process involves the catalytic reactions with water and alcohol, or water and organic acid. The reaction between catalyst and water is especially critical. Without the existence of water to participate, hydrogen does not produce. From Table 4, the highest H_2 yield of 7.65 $mmol{\cdot}g^{-1}catal.{\cdot}h^{-1}$ in the methanol solution and 9.45 $mmol{\cdot}g^{-1}catal.{\cdot}h^{-1}$ in the ethanol solution, are much higher than that of CuOS at 0.270 $mmol{\cdot}g^{-1}catal.{\cdot}h^{-1}$. The H_2 generation also occurred for Cu*Mn*OS-0 with the yield of 2.17 $mmol{\cdot}g^{-1}catal.{\cdot}h^{-1}$ in an ethanoic acid solution. Under the 150 W Halogen lamp visible illumination, the H_2 yield degraded to 2.04 $mmol{\cdot}g^{-1}catal.{\cdot}h^{-1}$ in methanol solution. The ineffectiveness of photo-induced electron-hole pairs under light illumination for H_2 production at NTP indicates dehydrogenation of aqueous CH_3OH by Cu*Mn*OS-0 is not initiated by the electron/hole charges. After Cu*Mn*OS-0 nanoflower catalyst was annealed at 200 °C, its H_2 yield further degraded to 1.20 $mmol{\cdot}g^{-1}catal.{\cdot}h^{-1}$ due to the deactivation of the catalyst activity. There is a trend of lowering the H_2 yield at the higher Cu^+ content for preparing Cu*Mn*OS with the higher N_2H_4 amount. To test

catalyst reusability, Cu*Mn*OS-1 catalyst after the 24 h immersing in alcohol solution, drying, and re-filling was tested again and its H_2 yield of 6.63 mmol·g^{-1}catal.·h^{-1} was achieved.

H_2 evolution has been studied by different routes. For the photocatalytic reactions in the water/methanol solution, Sun *et al.* with Ni_2P/CdS nanorods obtained a record-high H_2 production rate of 553 mmol·g^{-1}catal.·h^{-1} under a filtered 300 W Xe lamp. The rate per input light power can be viewed as 1.84 mmol·g^{-1}catal.·h^{-1}·$watt^{-1}$[44]. The other excellent catalyst was Sr-$NaTaO_3$ with a rate of 48.9 mmol·g^{-1}catal.·h^{-1} or 0.79 mmol·g^{-1}catal.·h^{-1}·$watt^{-1}$[45]. Ruthenium hydride complex performed the best for the homogeneous catalysis of methanol and water into CO_2 and H_2O at 90 °C under the additive of KOH[7]. Without the precious metal, the H_2 production rate is low. Our Cu*Mn*OS-1 with a rate of 9.45 mmol·g^{-1}catal.·h^{-1} in the dark is encouraging.

Discussion

The developments of the pure electron-transport catalyst for reduction/hydrogenation of CO_2 into methanol and the pure hole-transport one for oxidation/dehydrogenation of aqueous alcohol into H_2 without the thermal, electrical, and photo energies are our major goals. We adopt the hexavalent Cr reduction and dye degradation for screening the redox capability during our search for catalysts. Compared with the reported redox reactions for the pollutant removal, our catalytic reactions are pretty fast at NTP. To further test the redox capability with our Cu*Mn*OS system, aqueous CO_2 hydrogenation is used for testing the catalytic reduction reaction and aqueous CH_3OH dehydrogenation for oxidation one. The first evidence for the success in the hydrogenation-dehydrogenation redox reactions is the content of the different Cu charge states. The [Cu^+]-high Cu*Mn*OS is used and good for CO_2 reduction, therefore it can transport electrons through the Cu^+/Cu^{2+} charge centers for the solution/catalyst interface reaction. The [Cu^+]-low Cu*Mn*OS is used for aqueous CH_3OH dehydrogenation, therefore it can transport holes through the Cu^+/Cu^{2+} charge centers.

For CH_3OH generation from the simple Cu*Mn*OS-CO_2-H_2O system, the formation of proton is needed, followed by the reaction with CO_2 for forming CH_3OH. For H_2 generation from the simple Cu*Mn*OS-CH_3OH-H_2O system at NTP, it needs any one of CH_3OH, H_2O, and Cu*Mn*OS added to the mixture of the other two, otherwise there is no H_2 gas release. This observation gives a hint that a series reaction operates in this system. To logically explain the complex reactions in each of the simple systems, our catalyst has to be quite active and can react in the CO_2-H_2O or CH_3OH-H_2O solution with H_2O existing in both situations. To make the series reaction happen and to explain the rare phenomena, the catalyst has to firstly react with H_2O, followed by the reaction with CO_2 in the Cu*Mn*OS-CO_2-H_2O system or with CH_3OH in the Cu*Mn*OS-CH_3OH-H_2O one, as we had mentioned about the critical role of H_2O. For catalyst to be active, its lattice bonding on surface needs to be weak for the interfacial exchange reactions. The degraded performance for the 200 °C-annealed Cu*Mn*OS in Table 4 is a support related to lattice bonding. Therefore, the second key factor for the success in the redox reactions is the weakened lattice oxygen at the catalyst surface to have its active lattice oxygen easily react with water for forming the oxygen vacancy and the oxidized OH^- on catalyst surface. The Kröger–Vink notation originally developed for ionic compounds is used here. For the oxygen vacancy ($V^{2+}_{O,lattice}$) as an example, the main body of V represents for vacancy, the subscript for the host lattice site, and the superscript for the relative charge. Here we adopted the positive charge of 2+ instead of the "••" symbol in the original invention. For the active lattice oxygen, it is shown as$O^0_{O,lattice}$. Therefore, *water* oxidation reaction is shown below in term of the Kröger–Vink notation:

$$H_2O_{(l)} + O^0_{O,lattice} = 2OH^-_{(adsorb.)} + V^{2+}_{O,lattice} \quad (1)$$

In the above Eq. 1, the mass, charge, and lattice site are required to be conservative. The active lattice oxygen on surface and the generated oxygen vacancy become the oxidant and the reducing agents, respectively. The redox reactions by oxide defects in CeO_2 had been used for thermochemical catalytic production of solar fuels above 1000 °C[46,47]. Here we just perform the similar reactions in the liquid state at much lower temperature. Before discussing the CO_2 hydrogenation and CH_3OH dehydrogenation, a common reaction in the Cu^{2+}/Cu^+ -coexisting compounds is listed below for the consideration of the reaction reversibility:

$$2Cu^0_{Cu} \overset{V^{2+}_O}{\longleftrightarrow} 2Cu^-_{Cu.} + V^{2+}_{O,lattice} \quad (2)$$

where Cu^-_{Cu} represents for the occupation of Cu^+ on the Cu^{2+} lattice site with a relative negative charge of 1- and Cu^0_{Cu} for the Cu^{2+} on the Cu^{2+} lattice site.

For the [Cu^+]-high Cu*Mn*OS-CO_2-H_2O reaction system to form CH_3OH at NTP, the reducing agent of oxygen vacancy can be oxidized by H_2O to form the active lattice oxygen on catalyst and 2 H^+ at the solid/liquid interface (Equation 3). The protons together with the hopping electrons between Cu^+ and Cu^{2+} in the [Cu^+]-high Cu*Mn*OS, shown in Eq. 4, can reduce the dissolved and adsorbed CO_2 into CH_3OH by the catalyst/solution interface reaction in Eq. 5. After combining Eqs. 2, 3, 4, and 5, the net equation 6 is obtained. Consistent with the data in Table 3, the mechanism explains that the increased Cu^+ content favors the electron formation in Eq. 4 and the CH_3OH yield in Eq. 5. Aided by $V^{2+}_{O,lattice}$ in Eq. 6, the formed $O^0_{O,lattice}$ can continuously proceed Eq. 1 to have the reversible reaction and the Cu*Mn*OS catalyst has its surface kept at dynamic equilibrium between $V^{2+}_{O,lattice}$ and $O^0_{O,lattice}$.

$$H_2O_{(l)} + V^{2+}_{O,lattice} = 2H^+_{(adsorb.)} + O^0_{O,lattice} \quad (3)$$

$$Cu^+ = Cu^{2+} + e^- \quad (4)$$

$$CO_2(aq.) + 6H^+_{(adsorb.)} + 6e^- = CH_3OH_{(aq.)} + H_2O_{(l)} \quad (5)$$

$$CO_{2\,(aq.)} + 2H_2O_{(l)} \overset{3V_O^{2+}}{\longleftrightarrow} CH_3OH_{(aq.)} + 3O^{0+}_{O,lattice} \quad (6)$$

The kinetic reaction steps in Eqs. 1 and 3 demonstrate the lattice oxygen in and out at the catalyst/solution interface to hold the dynamic equilibrium and to keep Cu*Mn*OS behave as a catalyst for a long period of reaction and for repeated use without being exhausted. For the reaction to continuously run, the continuous supply of electrons for Eq. 4 is needed. The establishment of thermal equilibrium in Eq. 2 is also important to avoid the electron depletion.

For the [Cu^+]-low Cu*Mn*OS-CH_3OH-H_2O reaction system to form H_2 at NTP, the reduced oxygen vacancy reacts with H_2O for *water* reduction to form H_2, two electrical holes ($2h^+$), and active lattice oxygen, as shown in Eq. 7. The hydroxyl group from Eq. 1 together with the hopping holes between Cu^+ and Cu^{2+} in the [Cu^+]-low Cu*Mn*OS, shown in Eq. 8, can oxidize CH_3OH into $5/2H_2$ and CO_2, as shown in Eq. 9. After combining Eqs. 1, 7, and 9, the net equation 10 is obtained. With this proposed mechanism, it can explain the fact that the aqueous methanol dehydrogenation cannot occur without the initiation of the water oxidation reaction in Eq. 1. It also explains the increased Cu^+ content unfavors the hole formation in Eq. 8 and the H_2 yield in Eq. 9, as supported by the data in Table 4.

$$H_2O_{(l)} + V^{2+}_{O,lattice} = H_{2\,(g)} + O^0_{O,lattice} + 2h^+ \quad (7)$$

$$Cu^{2+} = Cu^+ + h^+ \quad (8)$$

$$CH_3OH_{(l)} + OH^-_{(adsorb.)} + h^+ = \frac{5}{2}H_{2\,(g)} + CO_{2\,(g)} \quad (9)$$

$$CH_3OH_{(l)} + H_2O_{(l)} = 3H_{2\,(g)} + CO_{2\,(g)} \quad (10)$$

Thermodynamic consideration for the CO_2 hydrogenation is evaluated to support the feasibility of the reaction in Eq. 6, which can be divided into Eqs. 11 and 12:

$$CO_2(aq.) + 2H_2O_{(l)} = CH_3OH_{(aq.)} + \frac{3}{2}O_{2\,(g)} \quad (11)$$

$$\frac{3}{2}O_2(g) \overset{3V_O^{2+}}{\longleftrightarrow} 3O^0_{O,lattice} \quad (12)$$

The standard Gibbs free energies of formation of aqueous methanol, $O_{2(g)}$, $CO_{2(aq.)}$, and $H_2O_{(l)}$ are −174.5, 0, −386.2, and −237.14 kJ/mol[48]. The standard Gibbs free energy change of the reaction in Eq. 11 can be calculated to be $\Delta G_1^o = 685.98$ kJ/mol, related to a thermodynamic uphill and unfavorable reaction. For the reaction in Eq. 12, it behaves as the oxygen from the gas state to the metal oxide solid state with the release energy equal to the bond energy. Cu-O bond energy of 272.86 kJ/mol is reported[49]. If well-crystalline Cu*Mn*OS has the oxygen bond energy of 272.86 kJ/mol, we assume that the weakened oxygen bond energy in Cu*Mn*OS is 90% of 272.86 kJ/mol or the reaction energy change for one molar $O^0_{O,lattice}$ is $\Delta G_2^o = -245.88$ kJ/mol. Therefore, the net standard Gibbs free energy of the reaction in Eq. 6 is $\Delta G_1^0 + 3 \times \Delta G_2^o = -50.76$ kJ/mol, favorable for the reaction in Eq. 6 to occur. From this explanation, the consideration of the chemical potential of lattice oxygen is very important. The schematic diagram for the chemical reaction paths for CO_2 and H_2O to form methanol w/o catalyst is shown in Figure 7.

Similar to CO_2 hydrogenation, the catalytic reaction for aqueous methanol dehydrogenation can be calculated to be $\Delta G_3^o = 9.06$ kJ/mol for its net standard free energy change of reaction in Eq. 13, using the standard Gibbs free energies of formation of $H_{2(g)}$, $CO_{2(g)}$, $CH_3OH_{(l)}$, and $H_2O_{(l)}$ of 0, −394.38, −166.3, and −237.14 kJ/mole. The gas pressure deviation from the standard state of 1 atm can lead to the free energy change of $\Delta G_4 = RT\ell n\frac{P_1}{1}$ for Eq. 14 and $\Delta G_5 = RT\ell n\frac{P_2^3}{1} = 3RT\ell nP_2$ for Eq. 15. If P_1 is 0.01 atm for $CO_{2(g)}$ and P_2 0.03 atm for $H_{2(g)}$, ΔG_4 for Eq. 14 is −11.41 kJ/mol and ΔG_5 for Eq. 15 −26.06 kJ/mol. The net standard Gibbs free energy of the reaction in Eq. 10 is $\Delta G_3 + \Delta G_4 + \Delta G_5 = -28.41$ kJ/mol, favorable for the reaction in Eq. 10 to occur.

$$CH_3OH_{(l)} + H_2O_{(l)} = 3H_{2\,(g)}(1\text{ atm}) + CO_{2\,(g)}(1\text{ atm}) \quad (13)$$

$$CO_{2\,(g)}(1\text{ atm}) = CO_{2\,(g)}(P_1\text{ atm}) \quad (14)$$

$$3H_{2\,(g)}(1\text{ atm}) = 3H_{2\,(g)}(P_2\text{ atm}) \quad (15)$$

The achievements in CO_2 hydrogenation and aqueous CH_3OH dehydrogenation at 25 °C indicate our [Cu^+]-high and [Cu^+]-low Cu*Mn*OS catalysts have provided the different interfacial reactions to alter the reaction paths and to obtain fuels without additional inputs of energies and reagents.

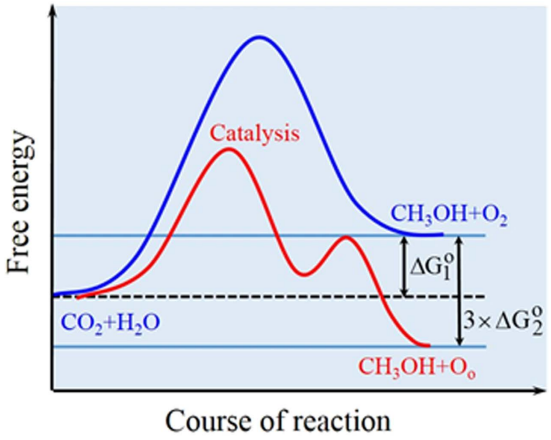

Figure 7. Reaction path in terms of reaction energy for CO_2 and H_2O to form methanol w/o catalyst.

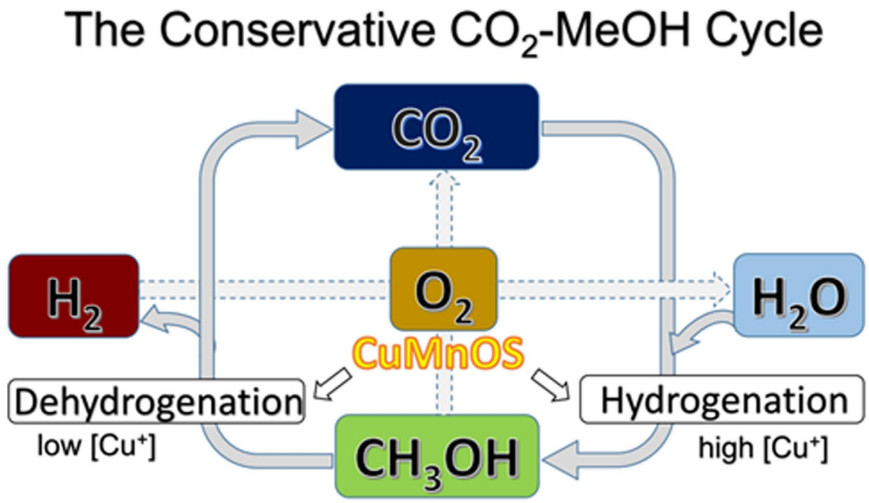

Figure 8. Schematic illustration of the conservative CO_2-CH_3OH cycle at normal temperature and pressure.

The charge transfer between Cu^+ and Cu^{2+} in semiconductor to provide the electron transport for the n-type or the hole transport for the p-type is understandable. The active lattice oxygen is the key factor for the success of the aqueous CO_2 reduction and aqueous CH_3OH dehydrogenation. Basically, ceramic catalysts have long been viewed to be activated at high temperature but cannot at NTP in water. Here our proposed reaction mechanism of Cu*Mn*OS in water for redox reactions at NTP is similar to that of CeO_2 in water vapor at high temperature with the basis of oxygen vacancy[46]. The thermodynamic calculation also supports the occurrence of the redox reactions. The realization of our CO_2-CH_3OH cycle at NTP is strongly related to the reactions between catalyst and water (Equation 1), which are attributed to the low processing temperature for Cu*Mn*OS, the S^{6+} -O bond formation, and the substitution of Mn for Cu to distort the lattice, to weaken the lattice O bonds, and to form the active lattice oxygen. The degraded performance in the H_2 yield for the 200 °C-annealed Cu*Mn*OS in Table 4 is related to the stronger bonding to deactivate the lattice oxygen for Eq. 1. The photo-excitation result in Table 4 also supports the water oxidation by catalyst as the first reaction step instead of the electron/hole-activated reaction. The weakening of the oxygen bonding to initiate catalytic reactions can be the design strategy for inorganic or heterogeneous catalysts to increase their catalytic activity at mild condition.

Figure 8 is the schematic illustration to show the conservative CO_2-CH_3OH cycle. With the $[Cu^+]$-high Cu*Mn*OS catalyst, the greenhouse CO_2 gas can be recycled and re-utilized by catalytic reduction reaction together with water to form aqueous CH_3OH solution as the hydrogen liquid carrier, fuel, or the chemical feedstock. With the $[Cu^+]$-low Cu*Mn*OS, aqueous CH_3OH solution can be instantaneously dehydrogenated into H_2 and CO_2. Both CH_3OH and H_2 are important energy carriers and chemical precursors. The instantaneous H_2 generation from the CH_3OH solution can be feasibly applied to the portable appliance, transportation vehicles, power plants etc., after methanol safety has been well considered. The products of CO_2/H_2O from the combustion of CH_3OH/H_2 can be again recycled and re-utilized. This CO_2-CH_3OH cycle occurred at NTP is conservative and renewable.

In summary, we demonstrate the nanoflower-like Cu*Mn*OS catalyst system to complete the conservative CO_2-CH_3OH hydrogenation-dehydrogenation cycle in an aqueous solution at normal temperature and pressure without additional energy inputs and reagents. This catalyst system has two different forms. The [Cu^+]-high Cu*Mn*OS can transport electrons and is used for the aqueous CO_2 hydrogenation to CH_3OH at a yield of 21.1 mmol·g^{-1}catal.·h^{-1}. It is the [Cu^+]-low Cu*Mn*OS to transport holes and to instantaneously dehydrogenize aqueous CH_3OH solution into H_2 at a yield of 7.65 mmol·g^{-1} catal.·h^{-1}. In additional to the electron and hole charges, the key factor in completing the CO_2-CH_3OH cycle is the active lattice oxygen of Cu*Mn*OS to firstly initiate water oxidation at the catalyst-water interface. The bond weakening concept in forming the active lattice oxygen opens a route to increase the catalytic activity of inorganic catalysts for redox reactions at mild condition. The H_2 liquid carrier of aqueous CH_3OH solution with instantaneous H_2 liberation can provide wide applications in portable appliance, vehicle transportation, power plant etc.

References

1. Olah, G. A. After oil and gas: methanol economy. *Catal. Lett*. **93,** 1–2 (2004).
2. Olah, G. A., Prakash, G. K. S. & Goeppert, A. Anthropogenic chemical carbon cycle for a sustainable future. *J. Am. Chem. Soc*. **133,** 12881–12898 (2011).
3. Lee, S., Speight, J. G. S. & Loyalka, K. In *Handbook of alternative fuel technology*. CRS Press, Taylor & Francis Group, 2007.
4. Jadhav, S. G., Vaidya, P. D., Bhanage, B. M. & Joshi, J. B. Catalytic carbon dioxide hydrogenation to methanol: a review of recent studies, *Chem. Eng. Res. design* **92,** 2557–2567 (2014)
5. Bahruji, H. *et al.* Pd/ZnO catalysts for direct CO_2 hydrogenation to methanol. *J. Catal*. (2016) *in press*, doi: 10.1016/j.jcat.2016.03.017.
6. Studt, F. *et al.* Discovery of a Ni–Ga catalyst for carbon dioxide reduction to methanol. *Nat. Chem*. **6,** 320–324 (2014).
7. Alberico, E. & Nielsen, M. Towards a methanol economy based on homogeneous catalysis: methanol to H_2 and CO_2 to methanol. *Chem. Commun*. **51,** 6714–6725 (2015).
8. Huff, C. A. & Sanford, M. S. Cascade catalysis for the homogeneous hydrogenation of CO_2 to methanol. *J. Am. Chem. Soc*. **133,** 18122–18125 (2011).
9. Wesselbaum, S., Stein T. V., Klankermayer, J. & Leitner, W. Hydrogenation of carbon dioxide to methanol by using a homogeneous ruthenium–phosphine catalyst. *Angew. Chem. Int. Ed.* **51,** 7499–7502 (2012).
10. Liu, S. Q. *et al.* An artificial photosynthesis system based on CeO_2 as light harvester and N-doped graphene Cu(II) complex as artificial metalloenzyme for CO_2 reduction to methanol fuel. *Catal. Commun*. **73,** 7–11 (2016).
11. Tsai, C. W., Chen, H. M., Liu, R. S., Asakura, K. & Chan, T. S. Ni@NiO core–shell structure-modified nitrogen-doped $InTaO_4$ for solar-driven highly efficient CO_2 reduction to methanol. *J. Phys. Chem. C* **115,** 10180–10186 (2011).
12. Yamashita, H. *et al.* Selective formation of CH_3OH in the photocatalytic reduction of CO_2 with H_2O on titanium oxides highly dispersed within zeolites and mesoporous molecular sieves. *Catal. Today* **45,** 221–227 (1998).
13. Palo, D. R., Dagle, R. A. & Holladay, J. D. Methanol steam reforming for hydrogen production. *Chem. Rev*. **107,** 3992–4021 (2007).
14. Navarro, R. M., Penã, M. A. & Fierro, J. L. G. Hydrogen production reactions from carbon feedstocks: fossil fuels and biomass. *Chem. Rev*. **107,** 3952–3991 (2007).
15. Sá, S., Silva, H., Brandão, L., Sousa, J. M. & Mendes, A. Catalysts for methanol steam reforming–A review. *Appl. Catal. B-Environ*. **99,** 43–57 (2010).
16. Rodriguez-Lugo *et al.* A homogeneous transition metal complex for clean hydrogen production from methanol–water mixtures. *Nat. Chem*. **5,** 342–347 (2013).
17. Nielsen, M. *et al.* Low-temperature aqueous-phase methanol dehydrogenation to hydrogen and carbon dioxide. *Nature* **495,** 85–89 (2013).
18. Lilac, A. A. & Paul, A. Photocatalytic hydrogen production with tunable nanorod heterostructures. *J. Phys. Chem. Lett.* **1,** 1051–1054 (2010).
19. Lingampalli, S. R., Gautam, K. U. & Rao, C. N. R. Highly efficient photocatalytic hydrogen generation by solution-processed ZnO/Pt/CdS, ZnO/Pt/$Cd_{1-x}Zn_xS$ and ZnO/Pt/$CdS_{1-x}Se_x$ hybrid nanostructures. *Energy Environ. Sci*. **6,** 3589–3594 (2013).
20. Jitputti, J., Suzuki, Y. & Yoshikawa, S. Synthesis of TiO_2 nanowires and their photocatalytic activity for hydrogen evolution. *Catal. Comm*. **9,** 1265–1271 (2008).
21. Jiang, Y. *et al.* Novel AgPd hollow spheres anchored on graphene as an efficient catalyst for dehydrogenation of formic acid at room temperature. *J. Mater. Chem. A* **4,** 657–666 (2016).
22. Idris, A., Hassan, N., Rashid R. & Ngomsik, A. F. Kinetic and regeneration studies of photocatalytic magnetic separable beads for chromium (VI) reduction under sunlight. *J. Hazard. Mater.* **186,** 629–635 (2011).
23. Ghijsen, J. *et al.* Electronic structure of Cu_2O and CuO. *Phys. Rev. B* **38,** 11322–11330 (1988).
24. Xu, Z. H., Yu, Y. Q., Fang, D., Liang, J. R. & Zhou, L. X. Simulated solar light catalytic reduction of Cr(VI) on microwave–ultrasonication synthesized flower-like CuO in the presence of tartaric acid. *Mater. Chem. Phys.* **171,** 386–393 (2016).
25. Kumar, D. R., Manoj, D., Santhanalakshmi, J. & Shim, J. J. Au-CuO core-shell nanoparticles design and development for the selective determination of vitamin B_6. *Electrochim. Acta* **176,** 514—522 (2015).
26. Biesinger, M. C. *et al.* Resolving surface chemical states in XPS analysis of first row transition metals, oxides and hydroxides: Cr, Mn, Fe, Co and Ni. *Appl. Surf. Sci*. **257,** 2717–2730 (2011).
27. Raj, A. M. E. *et al.* XRD and XPS characterization of mixed valence Mn_3O_4 hausmannite thin films prepared by chemical spray pyrolysis technique. *Appl. Surf. Sci*. **256,** 2920–2926 (2010).
28. Chen, X. Y., Kuo, D. H. & Lu, D. F. N-doped mesoporous TiO_2 nanoparticles synthesized by using biological renewable nanocrystalline cellulose as template for the degradation of pollutants under visible and sun light. *Chem. Eng. J* **295,** 192–200 (2016).
29. Haber, J., Machej, T., Ungier, L. & Ziolkowski, J. N-doped mesoporous TiO_2 nanoparticles synthesized by using biological renewable nanocrystalline cellulose as template for the degradation of pollutants under visible and sun light. *Solid State Chem.* **25,** 207–218 (1978).
30. Lin, A. W. C., Armstrong, N. R. & Kuwana, T. X-ray photoelectron/auger electron spectroscopy of tin and indium foils and oxides. *Anal. Chem.* **49,** 1228–1235 (1977).
31. Klein, J. C., Li, C. P., Hercules, D. M. & Black, J. F. Decomposition of copper compounds in X-ray photoelectron spectrometers. *Appl. Spectrosc.* **38,** 729–734 (1984).
32. Strohmeier, B. R., Leyden, D. E., Field, R. S. & Hercules, D. M. Surface spectroscopic characterization of $CuAl_2O_3$ catalysts. *J. Catal.* **94,** 514–530 (1985).
33. Perry, D. L. & Taylor, J. A. X-ray Photoelectron and auger spectroscopic studies of Cu_2S and CuS. *J. Mater. Sci. Lett.* **5,** 384–386 (1986).
34. Liu S. X. & Chen, X. Y. A visible light response TiO_2 photocatalyst realized by cationic S-doping and its application for phenol degradation. *J. Hazard. Mater.* **152,** 48–55 (2008).
35. Yoon, M., Seo, M., Jeong, C., Jang, J. H. & Jeon, K. S. Synthesis of liposome-templated titania nanodisks: optical properties and photocatalytic activities. *Chem. Mater.* **17,** 6069–6079 (2005).

36. Xu, Z. *et al.* Enhancement in photo-fenton-like degradation of azo dye methyl orange using TiO_2/hydroniumjarosite composite catalyst. *Environ. Eng. Sci.* **32,** 497–504 (2015).
37. Shaham-Waldmann, N. & Paz, Y. Beyond charge separation: The effect of coupling between titanium dioxide and CNTs on the adsorption and photo catalytic reduction of Cr(VI). *Chem. Eng. J.* **231,** 49–58 (2013).
38. Xiao, D., Dai, K., Qu, Y., Yin, Y. & Chen, H. Hydrothermal synthesis of α-Fe_2O_3/g-C_3N_4 composite and its efficient photocatalytic reduction of Cr(VI) under visible light. *Appl. Surf. Sci.* **358,** 181–187 (2015).
39. Dinda, D., Gupta, A. & Saha, S. K. Removal of toxic Cr(VI) by UV-active functionalized graphene oxide for water purification. *J. Mater. Chem. A* **1,** 11221–11228 (2013).
40. Hu, B., Guild, C. & Suib, S. L., Thermal, electrochemical, and photochemical conversion of CO_2 to fuels and value-added products. *J. CO_2 Util.* **1,** 18—27 (2013).
41. Molla, A., Sahu, M. & Hussain, S. Under dark and visible light: fast degradation of methylene blue in the presence of Ag–In–Ni–S nanocomposites. *J. Mater. Chem. A* **3,** 15616 –15625 (2015).
42. Molla, A., Sahu, M. & Hussain, S. Synthesis of tunable band gap semiconductor nickel sulphide nanoparticles: Rapid and round the clock degradation of organic dyes. *Sci. Rep.* **6,** 26034 (2016).
43. Shu, Q. W., Lan, J., Gao, M. X., Wang, J. & Huang, C. Z. Controlled synthesis of CuS caved superstructures and their application to the catalysis of organic dye degradation in the absence of light. *CrystEngComm* **17,1374**–1380 (2015).
44. Sun, Z., Zheng, H., Li, J. & Du, P. Extraordinarily efficient photocatalytic hydrogen evolution in water using semiconductor nanorods integrated with crystalline Ni_2P cocatalysts. *Energy Environ. Sci.* **8,** 2668–2676 (2015).
45. Sun, J., Chen, G., Pei, J., Jin, R., Wang, Q. & Guang, X. A simple approach to strontium sodium tantalite mesocrystals with ultra-high photocatalytic properties for water splitting. *J. Mater. Chem.* **22,** 5609—5614 (2012).
46. Smestad, G. P. & Steinfeld, A. Review: photochemical and thermochemical production of solar fuels from H_2O and CO_2 using metal oxide catalysts. *Ind. Eng. Chem. Res.* **51,** 11828—11840 (2012).
47. Wang, F., Wei, M., Evans, D. G. & Duan, X. CeO_2-based heterogeneous catalysts toward catalytic conversion of CO_2. *J. Mater. Chem. A* **4,** 5773–5783 (2016).
48. Bard, A. J., Roger P. & Jordan J. In *Standard Potentials in Aqueous Solution* Marcel Dekker Inc., New York, 1985).
49. Sun, S., Wang, Y. & Yang, Q. Density functional theory study of the methanol adsorption and dissociation on CuO (1 1 1) surface. *Appl. Surf. Sci.* **313,** 777–783 (2014).

Acknowledgements

This work was supported by the Ministry of Science and Technology of the Republic of China under grant number MOST 104-2221-E-011-169-MY3.

Author Contributions

X.C. executed all the experimental works except for H_2 production measurement. H.A. was responsible for measuring hydrogen yield by GC. D.H.K. conducted the materials design of catalysts, the research direction, and the explanations in kinetics and thermodynamics. X.C. and D.H.K. wrote and reviewed the manuscript. D.H.K obtained the funding.

Additional Information

Competing financial interests: The authors declare no competing financial interests.

How to cite this article: Chen, X. *et al.* Cu*Mn*OS Nanoflowers with Different Cu^+/Cu^{2+} Ratios for the CO_2-to-CH_3OH and the CH_3OH-to-H_2 Redox Reactions. *Sci. Rep.* **7**, 41194; doi: 10.1038/srep41194 (2017).

Publisher's note: Springer Nature remains neutral with regard to jurisdictional claims in published maps and institutional affiliations.

This work is licensed under a Creative Commons Attribution 4.0 International License. The images or other third party material in this article are included in the article's Creative Commons license, unless indicated otherwise in the credit line; if the material is not included under the Creative Commons license, users will need to obtain permission from the license holder to reproduce the material. To view a copy of this license, visit http://creativecommons.org/licenses/by/4.0/

© The Author(s) 2017